Research Article

Yeong Hwan Ko, Kyu Jin Lee, Fairooz Abdullah Simlan and Robert Magnusson*

Singular states of resonant nanophotonic lattices

Abstract: Fundamental effects in nanophotonic resonance systems focused on singular states and their properties are presented. Strongly related to lattice geometry and material composition, there appear resonant bright channels and non-resonant dark channels in the spectra. The bright state corresponds to high reflectivity guided-mode resonance (GMR) whereas the dark channel represents a bound state in the continuum (BIC). Even in simple systems, singular states with tunable bandwidth appear as isolated spectral lines that are widely separated from other resonance features. Under moderate lattice modulation, there ensues leaky-band metamorphosis, merging modal bands and resulting in offset dark states and reflective BICs along with transmissive BICs within a high-reflectance wideband. Rytov-type effective medium theory (EMT) is shown to be a powerful means to describe, formulate, and understand the collective GMR/BIC fundamentals in resonant photonic systems. Particularly, the discarded Rytov analytical solution for asymmetric fields is shown here to predict the dark BIC states essentially exactly for considerable modulation levels. The propagation constant of an equivalent EMT homogeneous film provides a quantitative evaluation of the eminent, oft-cited embedded BIC eigenvalue. The work concludes with experimental verification of key effects.

Keywords: bound states in the continuum; effective medium theory; guided-mode resonance; nanophotonics.

1 Introduction

Understanding of wave propagation in periodic systems is foundational for their utility in science and engineering.

*Corresponding author: Robert Magnusson, Department of Electrical Engineering, University of Texas at Arlington, Arlington, TX 76019, USA,
E-mail: magnusson@uta.edu. https://orcid.org/0000-0002-8584-0791
Yeong Hwan Ko, **Kyu Jin Lee**, **and Fairooz Abdullah Simlan**, Department of Electrical Engineering, University of Texas at Arlington, Arlington, TX 76019, USA

Thus, the properties of solid-state materials are explained with band theory modeling propagation of electron waves in periodic crystal lattices. Elementary Bragg diffraction reveals energy bands and band gaps and classification of materials as insulators and conductors [1]. Similar bands appear in three-dimensional (3D) dielectric lattices called photonic crystals [2]. The band structure determines how photon propagation is affected by frequency, polarization, and direction. It may be represented in the first Brillouin zone with the first and higher band gaps corresponding to Bragg reflections at increasing frequency [3]. Whereas 3D dielectric periodicity is challenging in experimental realization, there is much current interest in practical film-based 1D and 2D optical lattices with straightforward fabrication. Key physical properties of these elements are explained in terms of the structure of the second (leaky) photonic stopband and its relation to the symmetry of the periodic profile.

When the lattice is confined to a layer thereby forming a periodic waveguide, an incident optical wave may undergo a guided-mode resonance (GMR) on coupling to a leaky eigen-mode of the layer system [4–7]. Figure 1(a) models the simplest resonance system possible, namely a subwavelength 1D periodic lattice or grating. Under normal incidence, counter-propagating leaky modes form a standing wave in the lattice. As the modes interact with the lattice, they reradiate [8]. A schematic dispersion diagram is shown in Figure 1(b). The device works in the second stop band corresponding to the second-order lattice [9]. A given evanescent diffraction order can excite not just one but several leaky modes. To emphasize this point, in Figure 1(b) we show the stop bands for the first two TE modes. At each stop band, a resonance is generated as denoted in Figure 1(b). The fields radiated by these leaky modes in a lattice with a symmetric profile can be in phase or out of phase at the edges of the band [10]. At one edge, there is a zero-phase difference, and hence the radiation is enhanced (GMR) while at the other edge, there is a π phase difference inhibiting the radiation. In this case, if $\beta = \beta_R + i\beta_I$ is the complex propagation constant of the leaky mode, $\beta_I = 0$ at one edge, which implies that no leakage is possible at that edge marking the condition as a bound state in the continuum (BIC). For asymmetric lattice profiles, guided-mode resonance prevails at each band edge. Fundamentally,
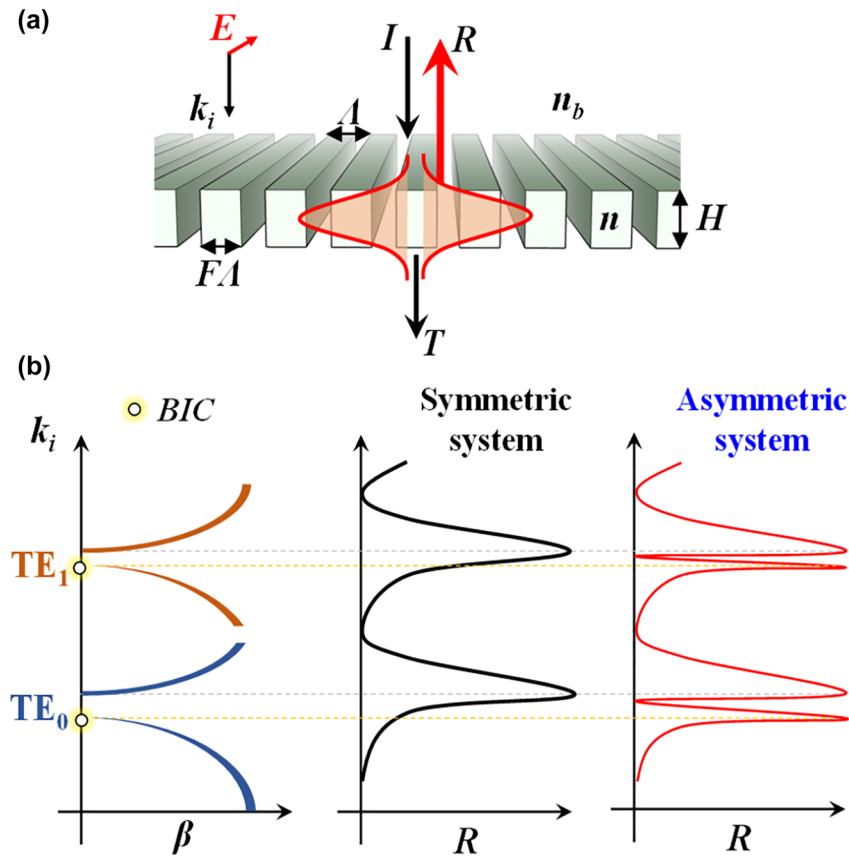
Figure 1: Lattice resonances in symmetric and asymmetric optical systems. (a) A schematic view of the simplest subwavelength resonance system. The model lattice has thickness (H), fill factor (F), period (Λ), and refractive indices of background and lattice material (n_b, n). When phase matching occurs between evanescent diffraction orders and a waveguide mode, a guided-mode resonance occurs. I, R, and T denote the incident wave with wavelength, reflectance, and transmittance, respectively. (b) A schematic dispersion diagram of a resonant lattice at the second stop band. For a symmetric lattice, the leaky edge supports guided-mode resonant radiation while the non-leaky edge hosts a non-radiant bound state. This picture applies to both TE (electric field vector normal to the plane of incidence and pointing along the grating grooves) and TM (magnetic field vector normal to the plane of incidence) polarization states. Here, the grating vector has magnitude $K = 2\pi/\Lambda$, $k_i = 2\pi/\lambda$, and β denotes a propagation constant of a leaky mode.

one-dimensional (1D) and 2D resonant lattices operate similarly and thus the description in Figure 1 applies generally.

Within the domain of nanophotonics, especially relating to new developments in metamaterials and metasurfaces, the resonance phenomena explained with Figure 1 are of major interest. The leaky (GMR) edge and the non-leaky (BIC) edge are inherent in resonance systems in this class. Historically, BICs were proposed in hypothetical quantum systems by von Neumann and Wigner [11]. In such systems, a completely bound state exists at an energy level above the lowest continuum level. Whereas the term BIC appeared in photonics in 2008 [12], the underlying concept was apparently first reported by Kazarinov et al. in 1976 [13]. These researchers derived a formula for the quality factor of a corrugated waveguide and reported zero radiation loss at the upper band edge when the second-order Bragg condition was satisfied. In a later paper, these effects

were elaborated with improved clarity [10]. Analyzing the second-order stop bands, Vincent and Neviere numerically demonstrated the existence of a non-leaky edge pertinent to symmetric gratings whereas asymmetric grating profiles yielded leaky radiant modes at both band edges [4]. Ding and Magnusson manipulated the separation of the non-degenerate leaky resonances associated with asymmetric profiles to engineer the resonant spectral response of periodic films [14]. Experimentally, the non-leaky edge was brought into view in 1998 by imposing asymmetry on an otherwise symmetric 1D periodic structure by variation of the incidence angle [15]; at the time the BIC terminology was not in use.

Reviewing briefly recent works, Marinica et al. proposed a symmetric double-grating structure to support embedded photonic bound states by coupling between two identical resonant grating layers [12]. Hsu et al. experimentally showed a diverging radiation Q factor as a

signature of embedded bound states in a 2D modulated layer of silicon nitride [16]. By tuning the structural symmetry or coupling strength between different resonance channels, quasi-BICs can be generated possessing ultranarrow linewidths [17–19]. Such high-Q resonances neighbouring BIC points enable ultra-sharp transmission and reflection spectra, yielding giant near-field enhancement and various promising applications including BIC-based chirality [20–22], lasing [23–25], nonlinearity [26–29], modulation [30] and sensing in various spectral regions [31]. In addition to the symmetry protected BICs in the Brillouin zone center at a Γ point, there exist off-Γ BIC states under non-normal incidence, sometimes called accidental BICs or quasi-BICs [32–40]; such BIC states provide additional degrees of freedom and application possibilities [41, 42].

In this paper, we treat leaky band metamorphosis where evolution of the leaky band structure with lattice modulation strength is evaluated. The resulting singular state is then shown to emerge as an isolated resonance feature brought to perfect narrowband reflection under broken symmetry. Effective-medium theory (EMT) based on the Rytov symmetric and asymmetric formalisms is shown to model the resonant and BIC states with high precision. The veracity of the Rytov EMT in delivering homogeneous waveguide slabs that contain the GMR/BIC resonance spectral properties is shown for practical modulation levels up to 3. Experimental results support the main theoretical conclusions.

2 Leaky-band metamorphosis

As in Figure 1(b) pertaining to a symmetric lattice, each resonant mode has a clear GMR leaky edge and a corresponding BIC nonleaky edge. This always holds for "weakly" modulated lattices. On increase of modulation, the band deviates and the GMR-BIC pairing is obscured. Key aspects of the band transformation can be brought out via the simple model in Figure 2(a). We compute incidence-angle (θ) dependent zero-order reflectance (R_0) in TE polarization. Figure 2(b) displays the $R_0(\theta, \lambda)$ map for $n = 1.4$ where the Rayleigh lines ($\lambda_R = \Lambda \pm \sin\theta$) are marked by white dashed lines. At normal incidence, a single R_0 peak appears at the upper band edge generated by symmetry-allowed GMR marked as s-GMR with the attendant leaky mode having a TE_0 mode shape. Meanwhile, at the opposite band edge, radiation is prohibited with a "dark state" appearing due to the symmetry-protected BIC (i.e., dark BIC). At nonnormal incidence under asymmetry, new R_0 peak branches form in the lower band denoted a-GMR also having a TE_0 mode character consistent with Figure 1(b) in low modulation. On approaching normal incidence and symmetry, the a-GMR vanishes becoming a BIC. Upon increasing n to 1.7, in Figure 2(c), the bandwidth of the high R_0 peak expands due to the strengthened dielectric modulation ($\Delta\varepsilon = n^2 - n_a^2$). Particularly, in the upper band, the high R_0 region is enlarged around the s-GMR within the λ_R lines achieving wideband reflection. The leaky modes forming
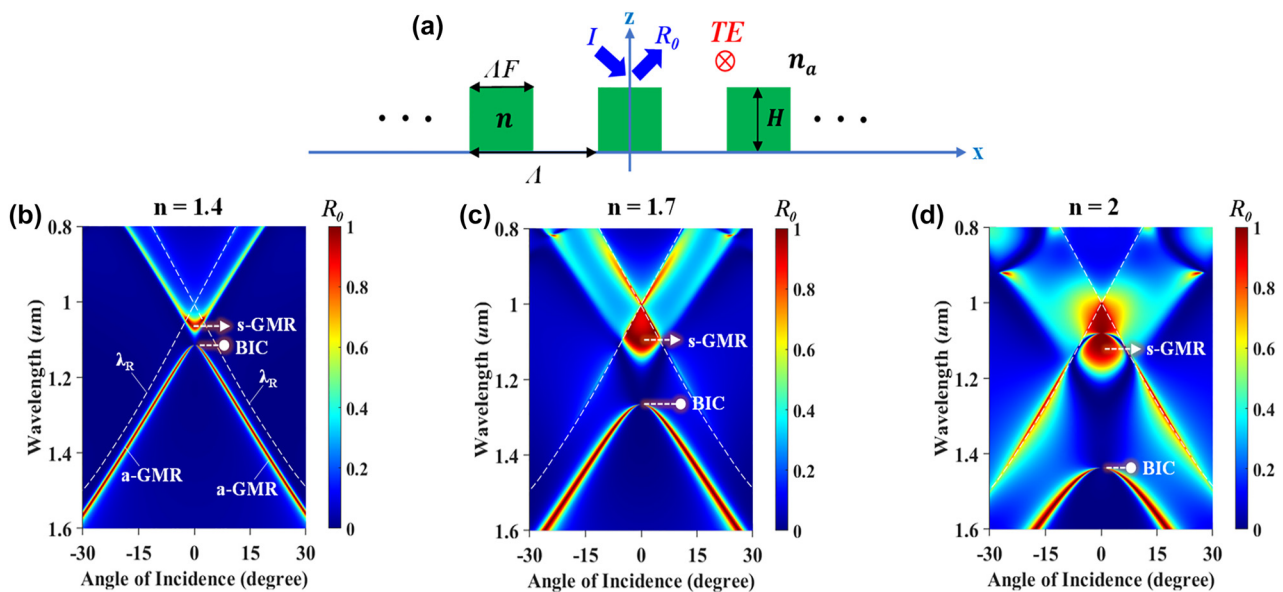

Figure 2: Leaky-band metamorphosis. (a) Modeling a simple subwavelength photonic lattice in air ($n_a = 1$). Parameters are period ($\Lambda = 1$ μm), grating width ($W = \Lambda F = 0.5$ μm) and height ($H = 0.5$ μm) under TE-polarized plane-wave incidence. Angular zeroth-order reflectance $R_0(\theta, \lambda)$ properties are analyzed with rigorous coupled wave analysis (RCWA) for lattice refractive indices (b) $n = 1.4$, (c) $n = 1.7$ and (d) $n = 2$. Note that, we use an inverted wavelength scale for consistency with proper band terminology where the upper band refers to high frequency. The Rayleigh wavelength (λ_R) is denoted by white dashed lines.

the contiguous high-reflection region at the upper band now have mixed TE_0 and TE_1 shapes while the lower band retains its TE_0 mode character. Beyond the λ_R lines, R_0 rapidly decreases because of leakage to higher-order reflection and transmission. Concomitantly, the band gap between the s-GMR and BIC states increases. In a prior study [43], we explain how the increase of $\Delta\varepsilon$ opens the band gap after band closure affected by the first and second Fourier harmonics of the dielectric function in the small-modulation limit. In the current example, the band gap closes near $n = 1.1$. On setting $n = 2$, in Figure 2(d), the reflectance bandwidth broadens further, and the band gap increases. Remarkably, the BIC state separates widely from other prominent resonance features and resides in an extensive, low-reflectance region. At $\theta = 0°$, the fundamental TE_0 mode is missing. Setting the angle to a small value brings out a sharp reflective resonance with $R_0 = 1$ mediated by the fundamental, now leaky, mode. The narrow-line resonance emerging from a dark background appears as a singular state in the spectrum. As an aside, in the upper band of Figure 2(d), a small incident angle induces a sharp resonant dip in the background of high reflection. Recently, such zero-order transmittance (T_0) spectra have been connected to electromagnetically induced transparency (EIT) as being EIT-like or EIT-analogous.

3 The singular state and its eigenvalue

We now analyze the singular state in detail. We show that it is possible to establish a homogeneous equivalent waveguide representing the resonant lattice nearly exactly. The propagation constant β of the leaky mode is then known and represents the embedded eigenvalue belonging to the unexcited bound state.

Figure 3(a) shows mode loci for the slab waveguide modes supported in the equivalent 1D lattice with refractive index $n = 2$, as displayed in Figure 2(a). To define the equivalent slab, the periodic layer is homogenized by effective medium theory (EMT) with the Rytov formalism in TE polarization [44, 45] expressed as
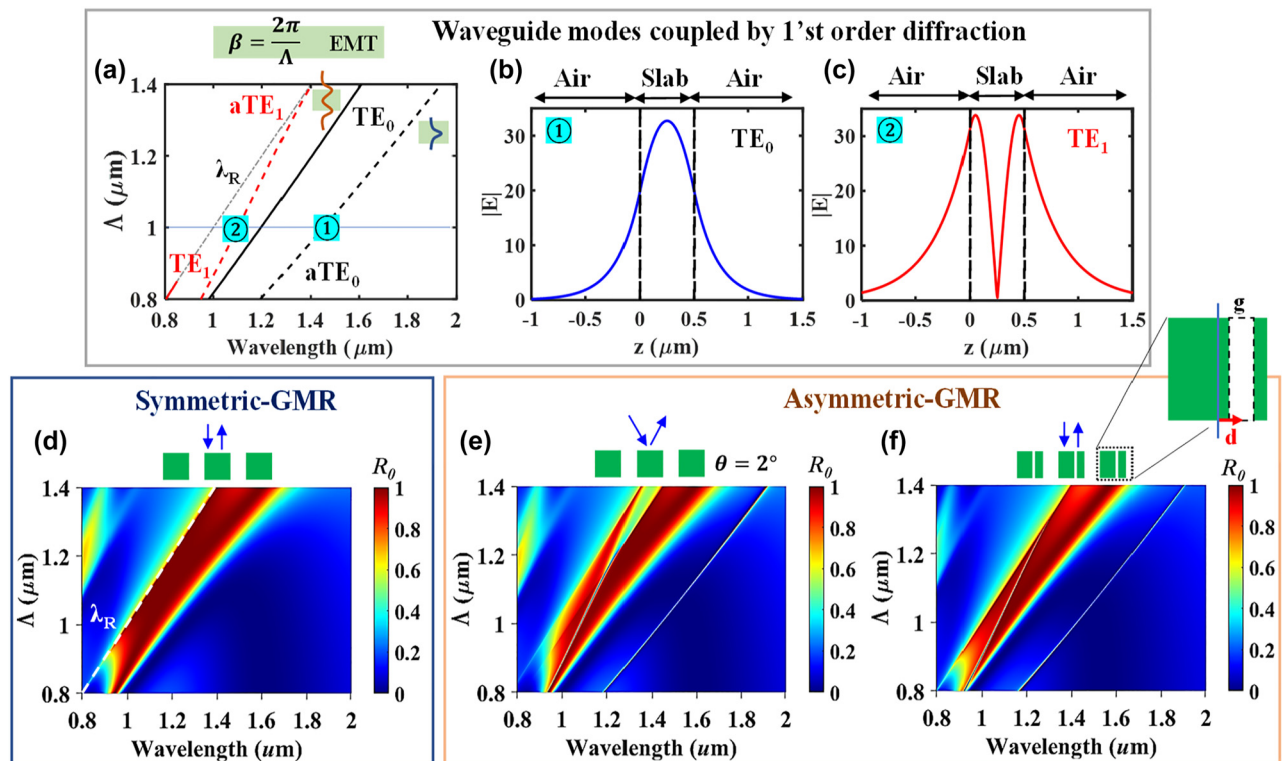

Figure 3: Analysis of phase matching to resonant states in symmetric and asymmetric optical lattices with $n = 2$. (a) Mode loci in the equivalent lattice homogenized by the Rytov EMT and thus becoming a slab waveguide. At points of ① and ②, with $\Lambda = 1$ μm, transverse profile of $|E|$ is calculated showing (b) TE_0 and (c) TE_1 mode shapes. The $R_0(\lambda, \Lambda)$ maps for (d) $\theta = 0°$, (e) $\theta = 2°$ and (f) asymmetric geometry at $\theta = 0°$ exhibit s-GMR and a-GMR features. In (f), the square rod is sliced by an air gap ($g = 0.05$ μm) where the distance between centers of rod and air gap is $d = 0.05$ μm.

$$\sqrt{1 - \left(n_{\mathrm{EMT}}^{\mathrm{TE}}\right)^2}\tan\left[\frac{\pi\Lambda}{\lambda}\left(n_a^2 - F\right)\sqrt{n_a^2 - \left(n_{\mathrm{EMT}}^{\mathrm{TE}}\right)^2}\right]$$

$$= -\sqrt{n^2 - \left(n_{\mathrm{EMT}}^{\mathrm{TE}}\right)^2}\tan\left[\frac{\pi\Lambda}{\lambda}F\sqrt{n^2 - \left(n_{\mathrm{EMT}}^{\mathrm{TE}}\right)^2}\right] \quad (1)$$

We use the first-order solution $n_1^{\mathrm{TE}}(\lambda, \Lambda)$ as an effective refractive index found by solving Eq. (1) corresponding to excitation by first-order diffracted waves. In his original 1956 paper, Rytov provided two solutions where one corresponded to complete symmetry represented by Eq. (1) of the local fields and the other to asymmetric fields [44]. He discarded the asymmetric solution as being unphysical and of no interest. But most importantly, the asymmetric local fields actually correspond to BIC states with the Rytov solution describing them with high precision as we now show. The discarded solution is [44].

$$\sqrt{1 - \left(v_{\mathrm{EMT}}^{\mathrm{TE}}\right)^2}\tan\left[\frac{\pi\Lambda}{\lambda}F\sqrt{n^2 - \left(v_{\mathrm{EMT}}^{\mathrm{TE}}\right)^2}\right]$$

$$= -\sqrt{n^2 - \left(v_{\mathrm{EMT}}^{\mathrm{TE}}\right)^2}\tan\left[\frac{\pi\Lambda}{\lambda}\left(n_a^2 - F\right)\right.$$

$$\left.\times\sqrt{n_a^2 - \left(n_{\mathrm{EMT}}^{\mathrm{TE}}\right)^2}\right] \quad (2)$$

From Eq. (2), we find $v_1^{\mathrm{TE}}(\lambda, \Lambda)$ corresponding to the effective index in the asymmetric case under leaky-mode excitation by the first evanescent diffraction order and use it to establish the equivalent homogeneous film. Then, we solve the classic slab waveguide eigenvalue problem for the qth TE mode using n_1^{TE} and v_1^{TE} [46].

$$\tan\left(\frac{n_1^{\mathrm{TE}}k_i H}{2} - \frac{\pi q}{2}\right) = \frac{\sqrt{(\beta)^2 - (n_a k_i)^2}}{n_1^{\mathrm{TE}}k_i} \quad \text{(Symmetric)}$$

$$(3)$$

$$\tan\left(\frac{v_1^{\mathrm{TE}}k_i H}{2} - \frac{\pi q}{2}\right) = \frac{\sqrt{(\beta)^2 - (n_a k_i)^2}}{v_1^{\mathrm{TE}}k_i} \quad \text{(Asymmetric)}$$

$$(4)$$

Here, in the slab, the propagation constant (β) equals the grating vector ($K = 2\pi/\Lambda$) under input wavevector ($k_i = 2\pi/\lambda$) on phase-matching to the first evanescent diffraction order.

In Figure 3(a), the solid lines show the mode loci for the symmetric situation found by Eqs. (1) and (3). In the plot, there are two TE modes under or near the Rayleigh $\Lambda = \lambda_R$ line where TE_0 and TE_1 denote the fundamental ($q = 0$) and first-order ($q = 1$) waveguide modes. For each mode, as shown in illustrative insets, the local field intensity is confined in a single (at film center) and double peak (near film edges) as typical in symmetric slab waveguides.

The asymmetric GMR modes similarly identified by solving Eqs. (2) and (4) in the slab waveguide are displayed by dashed lines in Figure 3(a). As explained in detail in [45] for guided-mode resonant lattices, operating with first-order diffraction ($m = 1$), the lattice is homogenized by vertical indices n_1^{TE} and v_1^{TE} with corresponding wave numbers $k_i n_1^{\mathrm{TE}}$ and $k_i v_1^{\mathrm{TE}}$ whereas lateral modes see $\beta = K$.

Figure 3(b) and (c) shows simulated magnitude distribution of the electric field ($|E|$) of TE_0 and TE_1 modes at $\Lambda = 1\,\mu\mathrm{m}$ where the corresponding λ locates at ① 1.531 μm and ② 1.153 μm. Figure 3(d) shows the $R_0(\lambda, \Lambda)$ map at normal incidence as computed exactly with rigorous coupled-wave analysis (RCWA) [47, 48] with 21 harmonics retained. Bounded by the λ_R line, a high R_0 band forms around the TE_1 and TE_0 mode lines in Figure 3(a). Thus, the characteristics and mode support picture of the EMT slab guide agree well with the rigorous numerical results. Figure 3(e) shows the $R_0(\lambda, \Lambda)$ map for the asymmetric case with $\theta = 2°$. The singular state locus is seen as a narrow high-reflection band offset from the other resonance features by l ~200 nm. It is predicted by the EMT model nearly exactly as seen by comparing with the aTE_0 locus in Figure 3(a). Similarly, the resonance line marked aTE_1 agrees well with the numerical map.

An alternate approach is to break the symmetry geometrically while maintaining normal incidence as noted in Figure 3(f) where similar spectra appear. To implement the asymmetric geometry, each rod is asymmetrically sliced by an air gap ($g = 0.05\,\mu\mathrm{m}$) where the cutting position ($d = 0.05\,\mu\mathrm{m}$) is decided by the distance between the center of the ridge and the air gap. In the $R_0(\lambda, \Lambda)$ maps, sharp resonances appear near the modal curves of Figure 3(a) and generally exhibit a Fano line shape. As the a-GMR is induced in broken symmetry under phase-matching, there open radiation channels with pathways in both transmission and reflection. The channel at the aTE_0 mode location produces a narrow-band perfect reflection $R_0 = 1$ whereas the one at aTE_1 appears in the wide-reflectance band and produces a sharp transmission $T_0 = 1$ peak or "BIC-EIT." Comparing Figure 3(a) to Figure 3(e) and (f) shows, quite surprisingly, that the discarded Rytov solution in Eq. (2) predicts the BIC state essentially exactly. The embedded eigenvalue of the aTE_0 mode corresponding to the reflective BIC state is $\beta(\lambda) = K = 2\pi/\Lambda$ and is thus given numerically in Figure 3(a).

Figure 4 verifies the a-GMR spectral identity. In Figure 4(a), two R_0 spectra are given by horizontal crosscuts of Figure 3(d) and (e) at $\Lambda = 1\,\mu\mathrm{m}$. In the plot, at $\theta = 2°$, two sharp peaks locate at ① $\lambda = 1.441\,\mu\mathrm{m}$ and ② 1.084 μm in the broken symmetry. For each position, corresponding
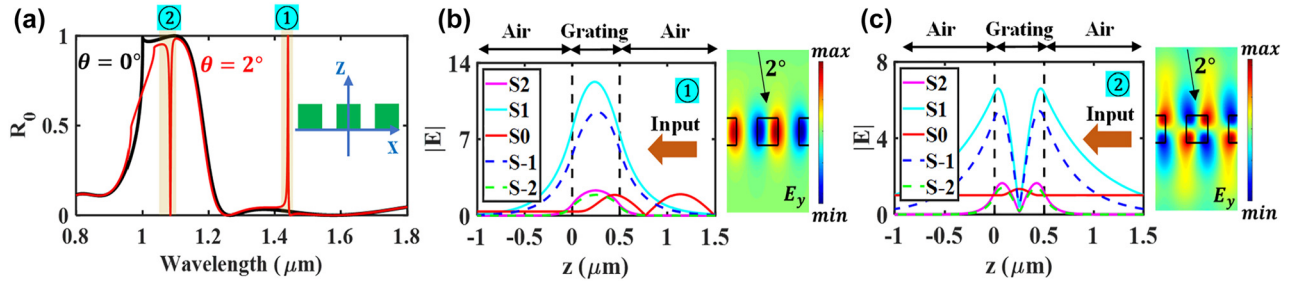
Figure 4: Resonance spectra and leaky-mode profiles under a-GMR. (a) R_0 spectra at $\theta = 0°$ and $\theta = 2°$ of the model 1D optical lattice {$\Lambda = 1$ μm, $F = 0.5$, $H = 0.5$ μm, $n = 2$} at a crosscut of Figure 4(d) and (e) at $\Lambda = 1$ μm. For a-GMR reflectance peak and null at ① and ②, the corresponding leaky-mode and electric-field profiles are presented in (b) and (c).

leaky-mode field profiles are characterized by RCWA in Figure 4(b) and (c) where $S_{\pm m}$ denote amplitudes of the coupled $\pm m$th diffraction orders. Comparing to Figure 3(b) and (c), we see that the modes driven by $S_{\pm 1}$ and $S_{\pm 2}$ match the reference TE_0 and TE_1 mode profiles, proving that the diffraction orders are coupled to the leaky waveguide modes in broken symmetry. Furthermore, these modes generate the attendant radiation channels. As seen in Figure 4(b), the S_0 is reflected along the $+Z$ direction (i.e., R_0) by the resonant interaction of the incident light with the TE_0 mode of the $S_{\pm 1}$ and $S_{\pm 2}$. On the other hand, in Figure 4(c), the S_0 passes through the lattice (i.e., T_0) after interfering with the TE_1 mode. As seen in the transverse electric field (E_y) maps in Figure 4(b) and (c), the standing wave patterns are asymmetric relative to the lattice.

4 Veracity of Rytov's solutions relative to lattice modulation

Figure 5 shows the band progression versus the refractive index modulation strength $\Delta\varepsilon = n_H^2 - n_L^2$ where the n_H and n_L are high and low refractive indices of the lattice. In Figure 5(a), the numerical R_0 loci at $\theta = 0°$ appear as s-GMR bands with TE_0 and TE_1 being the radiative leaky modes. The dark states can be tracked by slightly breaking the symmetry as shown in Figure 5(b). At $\theta = 0.1°$, two dark states are seen to gradually move to lower energy when $\Delta\varepsilon$ increases. One dark state remains in a bound state at longer wavelengths while the other locates in the high reflection band of the s-GMR TE_0 and TE_1 modes. Upon breaking the symmetry, in relatively strong modulation, each dark state is transferred to a narrow reflective GMR and EIT-GMR, respectively. Figure 5(c) confirms the veracity of the formulation of s- and a-GMRs with symmetric and asymmetric Rytov-type EMT. Each modal line in Figure 5(c) matches the numerical resonant leaky bands nearly perfectly.

5 Experimental results

The singular state is demonstrated by a silicon (Si) 1D lattice structure as shown in Figure 6(a). For facile device fabrication, avoiding the membranes in air presented in the theory sections above, we use crystalline Si (c-Si, $n_{Si} = 3.48$) on a quartz ($n_{Qz} = 1.45$) substrate and index matching oil ($n_{oil} = 1.45$) to reach vertical symmetry. After cleaning the SOQ wafer with a 620 nm-thick c-Si layer (Shin-Etsu Chemical, Co., Ltd.), we adjust the thickness of the c-Si layer by dry etching. Then, 1D c-Si grating patterns are prepared by UV laser interference lithography and a dry etching process [49]. Illuminating a coherent beam ($\lambda = 266$ nm) on a classic Lloyd's mirror, a spin-coated photoresist (PR, Shipley 1813) layer is inscribed with 1D patterns. With proper exposure time, the PR is patterned with desired fill factor. Then, the c-Si layer is etched in a reactive-ion etcher with $CHF_3 + SF_6$ gas mixture. After residual PR removal, a Si 1D grating on quartz substrate is prepared as depicted in the second step of Figure 6(a). To realize membrane-like structure, refractive index-matching oil (Cargille Lab. Series A) is placed on the Si grating. Thereafter, as seen in the fourth step, it is encapsulated with a bare quartz substrate. As seen in the photographic image, several 5 mm by 5 mm c-Si membrane cells are embedded in double quartz substrates. With the given large modulation strength ($\Delta\varepsilon = 3.48^2 - 1.45^2 = 10$), we designed these 1D membrane structures to exhibit new singular states. The fabricated c-Si membrane is characterized by an atomic force microscope (AFM) image and attendant profile. Figure 6(b) shows the T_0 spectra of a designed c-Si lattice for input angles $\theta = 0°$ and $2°$ where the grating parameter set ($\Lambda = 0.835$ μm, $F = 0.522$ and $H = 0.329$ μm) is optimized by performing particle swarm optimization (PSO) algorithm with RCWA [50]. As illustrated in the inset, we consider the refraction angle of incident light between air ($n_a = 1$) and quartz ($n_{Qz} = 1.45$). At off-normal incidence $\theta = 2°$
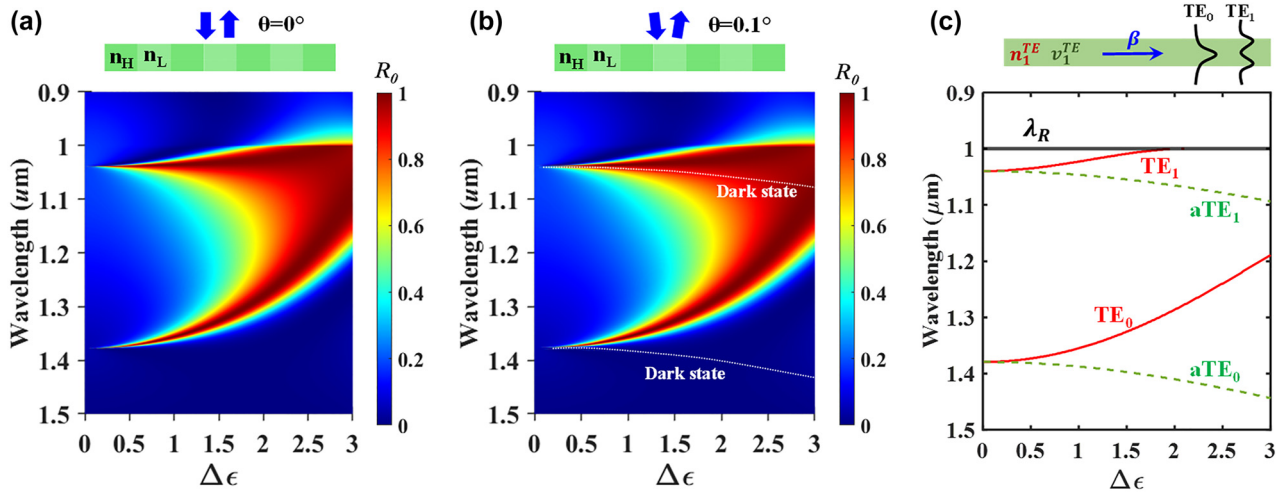
Figure 5: Band progression relative to index modulation strength $\Delta\epsilon = n_H^2 - n_L^2$. The lattice has parameters ($\Lambda = 1$ μm, $F = 0.5$ and $H = 0.5$ μm) while keeping a fixed average refractive index ($n_{avg} = \sqrt{Fn_H^2 + (1-F)n_L^2}$). Reflectance $R_0(\Delta\epsilon, \lambda)$ is found by RCWA at (a) normal incidence $\theta = 0°$ and (b) off-normal incidence $\theta = 0.1°$. In the symmetric system of (a), two (upper) modal bands appear. In (b), at slightly broken symmetry, two hidden dark states appear as lower bands. (c) Mode loci of the equivalent TE slab applying the symmetric and asymmetric Rytov EMT where the λ_R indicates the Rayleigh wavelength. As $\Delta\epsilon$ increases, the pair of bands split in symmetric and asymmetric GMRs, with an excellent match to (b). Interestingly, the lower band of the aTE$_0$ mode is highly separated from the upper band of the TE$_0$ mode, which leads to the isolated singular states of central importance.
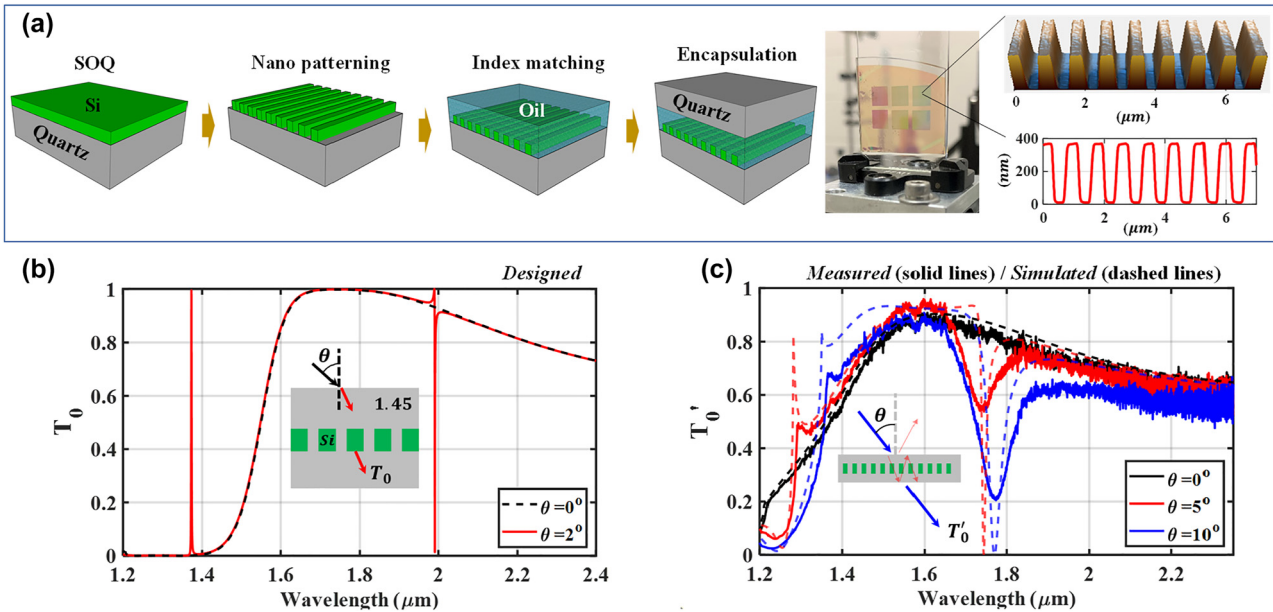

Figure 6: Experimental verification of the existence of singular states in simple resonant lattices. (a) Fabrication procedure of a Si membrane that includes four steps: preparing an SOQ wafer (crystalline Si on quartz), nanopatterning, refractive-index matching, and encapsulating. A photographic image shows the membrane cells embedded in two quartz substrates. The microscopic image and grating profiles are characterized with AFM measurements. (b) Design of c-Si ($n_{Si} = 3.48$) membrane in quartz ($n_{Qz} = 1.45$) to expose a singular state where the grating parameter set ($\Lambda = 0.835$ μm, $F = 0.522$ and $H = 0.329$ μm) is optimized by our PSO algorithm. In the T_0 spectra, the singular state and EIT-like resonance locate at $\lambda = 1.991$ and 1.373 μm under oblique incidence ($\theta = 2°$) in TE polarization. (c) Measured T_0' spectra (solid lines) for different incidence angles of $\theta = 0°$, 5° and 10° where the parameter set of the fabricated device is ($\Lambda = 0.835$ μm, $F = 0.396$ and $H = 0.33$ μm). For comparison, the simulated external T_0' spectra (dashed lines) are depicted for the same grating parameters.

under TE polarization, two a-GMRs appear as a singular state at $\lambda = 1.991\,\mu m$ and EIT-like resonance at $\lambda = 1.373\,\mu m$. The resonant signatures of the singular state and EIT-like state are observed in the fabricated device as presented in Figure 6(c). The grating parameter set of the fabricated c-Si membrane structure is ($\Lambda = 0.835\,\mu m$, $F = 0.396$ and $H = 0.33\,\mu m$) with the greatest deviation from the design parameters being in the fill Factor F. In the measured grating profile in the AFM image, in Figure 6(a), the surface roughness is approximately 5 nm. Sampling the device surface with AFM, the fill factor variation (F') is estimated as $F \pm 1.5\%$. To measure the spectral response, we use a near-IR spectrum analyzer (Yokogawa AQ6375) and a supercontinuum light source (SuperK COMPACT, NKT Photonics). Herein, the measured transmittance spectra (T'_0) are affected by substrate reflection, which is estimated by an analytical formula as explained in the Supplementary Materials. As represented in solid lines, the measured T'_0 spectra show the singular state clearly albeit with large linewidths. The EIT-like a-GMR at shorter wavelengths appears but somewhat weakly. Computing the spectra using the experimental parameters (dashed lines) shows a reasonably good match to the resonance positions of the measured T'_0 spectra. Due to the angular distribution in the input beam and imperfect fabrication, the bandwidth is broader, and efficiency is lower relative to theory. In more detail, the supercontinuum source is fiber coupled having somewhat spatially irregular output light distribution. An approximately collimated beam with ∼0.5 mm diameter is incident on the device. However, the distribution is not exactly Gaussian having angular components at angles >1°. Moreover, in the interference lithography system, there is a slight UV-laser intensity nonuniformity leading to a slow spatial variation in F. These effects are analyzed in some detail in the Supplementary Materials. In summary, by robust design and fabrication and by using well collimated Gaussian light beams, in analogous resonant systems, experimental results closely matching theoretical predictions can be achieved [51].

6 Conclusions

In summary, we have analytically and experimentally demonstrated singular states in simple optical lattices. These states appear as isolated, high-efficiency spectral lines arising out of a wideband low-reflectance floor and widely separated from other resonance features. In principle, these are perfectly reflecting BIC states under structural or angular asymmetric perturbation. Alternatively, they can be transmissive BICs within a high-reflectance wideband under

analogy with "electromagnetically induced transparency." In past research, we established the applicability of Rytov's full effective-medium theory (EMT) to the physical description and design of resonant optical lattices [45]. There, we applied the symmetric formalism to reliably describe the behavior of various optical devices such as wideband reflectors, resonant bandpass filters, and guided-mode resonance polarizers. Here, we additionally show the utility of Rytov's asymmetric solution that has hitherto not been known to be useful. We find that this rejected Rytov analytical EMT solution predicts the dark BIC states essentially exactly for substantial lattice modulation levels. Thus, the established equivalent BIC homogeneous waveguide slabs possess propagation constants that represent the embedded eigenvalues foundational to the BIC state. The resonant lattices analyzed numerically represent membranes that approximate silicon nitride hosted in air. The attendant fabrication is challenging as large-area membranes in air with nanoscale thickness tend to buckle and break due to local stresses. Thus, we apply silicon-on-quartz wafers with refractive-index matching oil to retain an approximately uniform host medium. The fabricated devices demonstrate key effects predicted here with reasonable agreement between experimental data and numerical evaluation using the experimental final parameters. The work presented herein addresses unexplored concepts in resonant nanosystems thereby laying groundwork for new scientific discoveries and applications.

References

[1] C. Kittel, *Introduction to Solid State Physics*, 4th ed. New York, Wiley, 1971.
[2] E. Yablonovitch, "Photonic band-gap structures," *J. Opt. Soc. Am. B*, vol. 10, p. 283, 1993.

[3] P. Markos and C. M. Soukoulis, *Wave Propagation: From Electrons to Photonic Crystals and Left-Handed Materials*, Princeton, Princeton University Press, 2008.

[4] P. Vincent and M. Neviere, "Corrugated dielectric waveguides: a numerical study of the second-order stop bands," *Appl. Phys.*, vol. 20, p. 345, 1979.

[5] L. Mashev and E. Popov, "Zero order anomaly of dielectric coated gratings," *Opt. Commun.*, vol. 55, p. 377, 1985.

[6] I. A. Avrutsky and V. A. Sychugov, "Reflection of a beam of finite size from a corrugated waveguide," *J. Mod. Opt.*, vol. 36, p. 1527, 1989.

[7] S. S. Wang and R. Magnusson, "Theory and applications of guided-mode resonance filters," *Appl. Opt.*, vol. 32, p. 2606, 1993.

[8] D. Rosenblatt, A. Sharon, and A. A. Friesem, "Resonant grating waveguide structure," *IEEE J. Quantum Electron.*, vol. 33, p. 203816, 1997.

[9] Y. Ding and R. Magnusson, "Band gaps and leaky-wave effects in resonant photonic-crystal waveguides," *Opt. Express*, vol. 15, p. 680, 2007.

[10] R. F. Kazarinov and C. H. Henry, "Second-order distributed feedback lasers with mode selection provided by first-order radiation loss," *IEEE J. Quantum Electron.*, vol. 21, p. 144, 1985.

[11] J. Von Neumann and E. Wigner, "Über merkwürdige diskrete Eigenwerte," *Phys. Z.*, vol. 30, p. 465, 1929.

[12] D. C. Marinica, A. G. Borisov, and S. V. Shabanov, "Bound states in the continuum in photonics," *Phys. Rev. Lett.*, vol. 100, p. 183902, 2008.

[13] R. F. Kazarinov, Z. N. Sokolova, and R. A. Suris, "Planar distributed-feedback optical resonators," *Sov. Phys. Tech. Phys.*, vol. 21, p. 131, 1976.

[14] Y. Ding and R. Magnusson, "Resonant leaky-mode spectral-band engineering and device applications," *Opt. Express*, vol. 12, p. 5661, 2004.

[15] Z. S. Liu, S. Tibuleac, D. Shin, P. P. Young, and R. Magnusson, "High-efficiency guided-mode resonance filter," *Opt. Lett.*, vol. 23, p. 1556, 1998.

[16] C. W. Hsu, B. Chen, J. Lee, et al., "Observation of trapped light within the radiation continuum," *Nature*, vol. 449, p. 188, 2013.

[17] K. Koshelev, S. Lepeshov, M. Liu, A. Bogdanov, and Y. Kivshar, "Asymmetric metasurfaces with high-Q resonances governed by bound states in the continuum," *Phys. Rev. Lett.*, vol. 121, p. 193903, 2018.

[18] B. Wang, W. Liu, M. Zhao, et al., "Generating optical vortex beams by momentum-space polarization vortices centred at bound states in the continuum," *Nat. Photonics*, vol. 14, p. 623, 2020.

[19] Z. Zhang, J. Yang, T. Du, H. Ma, and X. Jiang, "Tailoring bound states in the continuum in symmetric photonic crystal slabs by coupling strengths," *Opt. Express*, vol. 30, p. 8049, 2022.

[20] T. Shi, Z. L. Deng, G. Geng, et al., "Planar chiral metasurfaces with maximal tunable chiroptical response driven by bound states in the continuum," *Nat. Commun.*, vol. 13, p. 1, 2022.

[21] A. Overvig, N. Yu, and A. Alù, "Chiral quasi-bound states in the continuum," *Phys. Rev. Lett.*, vol. 126, p. 073001, 2021.

[22] W. Liu, B. Wang, Y. Zhang, et al., "Circularly polarized states spawning from bound states in the continuum," *Phys. Rev. Lett.*, vol. 123, p. 116104, 2019.

[23] C. Huang, C. Zhang, S. Xiao, et al., "Ultrafast control of vortex microlasers," *Science*, vol. 367, p. 1018, 2020.

[24] Y. Yu, A. Sakanas, A. R. Zali, E. Semenova, K. Yvind, and J. Mørk, "Ultra-coherent Fano laser based on a bound state in the continuum," *Nat. Photonics*, vol. 15, p. 758, 2021.

[25] M. S. Hwang, H. C. Lee, K. H. Kim, et al., "Ultralow-threshold laser using super-bound states in the continuum," *Nat. Commun.*, vol. 12, p. 4135, 2021.

[26] Fang, Q. Yang, Q. Yuan, et al., "Efficient second-harmonic generation from silicon slotted nanocubes with bound states in the continuum," *Laser Photonics Rev.*, vol. 16, p. 2100498, 2022.

[27] L. Carletti, K. Koshelev, C. De Angelis, and Y. Kivshar, "Giant nonlinear response at the nanoscale driven by bound states in the continuum," *Phys. Rev. Lett.*, vol. 12, p. 033903, 2018.

[28] H. K. Gandhi, D. Rocco, L. Carletti, and C. De Angelis, "Gain-loss engineering of bound states in the continuum for enhanced nonlinear response in dielectric nanocavities," *Opt. Express*, vol. 28, p. 3009, 2020.

[29] Z. Liu, Y. Xu, Y. Lin, et al., "High-Q quasibound states in the continuum for nonlinear metasurfaces," *Phys. Rev. Lett.*, vol. 123, p. 253901, 2019.

[30] T. C. Tan, Y. K. Srivastava, R. T. Ako, et al., "Active control of nanodielectric-induced THz quasi-BIC in flexible metasurfaces: a platform for modulation and sensing," *Adv. Mater.*, vol. 33, p. 2100836, 2021.

[31] Y. Wang, Z. Han, Y. Du, and J. Qin, "Ultrasensitive terahertz sensing with high-Q toroidal dipole resonance governed by bound states in the continuum in all-dielectric metasurface," *Nanophotonics*, vol. 10, p. 1295, 2021.

[32] J. W. Yoon, S. H. Song, and R. Magnusson, "Critical field enhancement of asymptotic optical bound states in the continuum," *Sci. Rep.*, vol. 5, p. 1, 2015.

[33] H. Hemmati and R. Magnusson, "Resonant dual-grating metamembranes supporting spectrally narrow bound states in the continuum," *Adv. Opt. Mater.*, vol. 7, p. 1900754, 2019.

[34] L. Liang, Q. Zheng, X. Nan, and Y. Dong, "Asymmetric all-dielectric active metasurface for efficient dual reflection modulation," *Opt. Commun.*, vol. 505, p. 127539, 2022.

[35] Z. Li, Q. Zhu, Y. Wang, and S. Xie, "Bound states in the continuum in the double-period rectangular hole arrays perforated in one layer of photonic crystal slab in the visible wavelength region," *Opt. Commun.*, vol. 436, p. 151, 2019.

[36] Y. Liang, K. Koshelev, F. Zhang, et al., "Bound states in the continuum in anisotropic plasmonic metasurfaces," *Nano Lett.*, vol. 20, p. 6351, 2020.

[37] Q. Zhou, Y. Fu, L. Huang, et al., "Geometry symmetry-free and higher-order optical bound states in the continuum," *Nat. Commun.*, vol. 12, p. 4390, 2021.

[38] M. Liu and D. Y. Choi, "Extreme huygens' metasurfaces based on quasi-bound states in the continuum," *Nano Lett.*, vol. 18, p. 8062, 2018.

[39] A. Cerjan, C. Jörg, S. Vaidya, et al., "Observation of bound states in the continuum embedded in symmetry bandgaps," *Sci. Adv.*, vol. 7, p. eabk1117, 2021.

[40] S. I. Azzam, V. M. Shalaev, A. Boltasseva, and A. Kildishev, "Formation of bound states in the continuum in hybrid plasmonic-photonic systems," *Phys. Rev. Lett.*, vol. 121, p. 253901, 2018.

[41] S. Han, M. V. Rybin, P. Pitchappa, Y. K. Srivastava, Y. S. Kivshar, and R. Singh, "Guided-mode resonances in all-dielectric terahertz metasurfaces," *Adv. Opt. Mater.*, vol. 8, p. 1900959, 2019.

[42] S. Han, P. Pitchappa, W. Wang, Y. K. Srivastava, M. V. Rybin, and R. Singh, "Extended bound states in the continuum with symmetry-broken Terahertz dielectric metasurfaces," *Adv. Opt. Mater.*, vol. 9, p. 2002001, 2021.

[43] S. G. Lee and R. Magnusson, "Band flips and bound-state transitions in leaky-mode photonic lattices," *Phys. Rev. B*, vol. 99, p. 045304, 2019.

[44] S. M. Rytov, "Electromagnetic properties of a finely stratified medium," *Sov. Phys. JETP*, vol. 2, p. 466, 1956.

[45] H. Hemmati and R. Magnusson, "Applicability of Rytov's full effective-medium formalism to the physical description and design of resonant metasurfaces," *ACS Photonics*, vol. 7, p. 3177, 2020.

[46] M. J. Adams, *An Introduction to Optical Waveguides*, New York, John Wiley & Sons, 1981.

[47] T. K. Gaylord and M. G. Moharam, "Analysis and applications of optical diffraction by gratings," *Proc. IEEE*, vol. 73, p. 894, 1985.

[48] M. G. Moharam, D. A. Pommet, E. B. Grann, and T. K. Gaylord, "Stable implementation of the rigorous coupled-wave analysis for surface-relief gratings: enhanced transmittance matrix approach," *J. Opt. Soc. Am. A*, vol. 12, p. 1077, 1995.

[49] K. J. Lee, J. Giese, L. Ajayi, R. Magnusson, and E. Johnson, "Resonant grating polarizers made with silicon nitride, titanium dioxide, and silicon: design, fabrication, and characterization," *Opt. Express*, vol. 8, p. 9271, 2014.

[50] J. Kennedy and R. Eberhart, "Particle swarm optimization," *Proc. IEEE Int. Conf. Neural Netw.*, vol. 4, p. 1948, 1995.

[51] J. Khüne, J. Wang, T. Weber, L. Khüner, S. A. Maier, and A. Tittl, "Fabrication robustness in BIC metasurfaces," *Nanophotonics*, vol. 10, p. 4305, 2021.